

Elastic Waves in Cylindrical Waveguides of Arbitrary Cross-Section

Vesna Damljanović and Richard L. Weaver
Theoretical and Applied Mechanics
University of Illinois at Urbana-Champaign

ABSTRACT

We consider wave propagation in slender elastic waveguides. With aim at finding all vibration modes of such bodies, we develop a theoretical framework for application of energy principles and subsequent discretization of the problem using the finite element method. We obtain a discrete set of solutions for propagating and evanescent branches and we examine the solution behavior in some detail. Finally, we compare the results with the analytic solutions of Pochhammer-Chree equations and conduct an accuracy and convergence study, determining the combination of mesh parameters and frequency regimes for which our code yields accurate results.

1. INTRODUCTION

Waveguides, as elastic slender bodies of constant cross-section with properties that are constant in preferred direction(s), are common in engineering practice. Accurate predictive capability regarding their vibrations and acoustics, followed by comparison with measurements, could be used for non-destructive evaluation (NDE) of such bodies. This includes material characterization, i.e., determination of the level of anisotropy, internal friction or contained stress. Ultrasonic inspection and acoustic emission from flaws also requires understanding of propagation in such bodies. The acoustics and vibrations of structures composed of plates, shells and beams can depend on understanding propagation in these components in more detail than is provided by simple strength of materials beam and plate theories.

The complexity of time-harmonic wave propagation in linear elastic waveguides arises from having two or more parallel boundaries that induce wave dispersion characterized by dependence of frequency or phase velocity on wavelength. Multiple reflections of elastic waves from the lateral boundaries lead to a complicated elastic wave field that is not easily analyzed in terms of the familiar P and S waves. In an infinite waveguide, however, translational invariance implies that each natural mode of vibration has single wavenumber k and corresponding simple variation (e^{ikz}) along the waveguide. While variations in the other direction(s) remain complicated, generally one expects a multi-branched dispersion relation.

The foundations for the contemporary studies of waveguides were laid by Pochhammer in 1876, and Rayleigh and Lamb in 1889. Pochhammer derived the general frequency equations for an infinite circular cylinder with a traction-free mantle and resolved it into various modes, while Rayleigh and Lamb derived the analogous equations for an infinite plate in plane strain and

traction-free faces [1]. From the abundance of literature on wave propagation in elastic rods and beams that stems from Pochhammer's work, in this paper we refer to but a few. In their work on dispersion of flexural waves Pao and Mindlin [2,3] constructed the approximate real and imaginary branches by analytically establishing a grid of boundary curves and asymptotic behavior. Onoe, McNiven and Mindlin [1, 4, 5] found the complete frequency spectrum for longitudinal waves in a circular rod including the complex branches. However, little attention has been given to wave propagation in rods of arbitrary cross-section, and even less detail has been analyzed regarding imaginary and complex branches of all the modes. Gavrić [6] developed a finite element technique for computation of full dispersion curves for the purpose of application in the high frequency regimes relevant for noise generation in rails. Though his formulation in principle enables calculation of imaginary and complex branches as well as real (which we verify in this paper), he doesn't obtain the complex and imaginary solutions or even describe the method he used for solving the final matrix equation. He focuses only on real branches, i.e. propagative modes, and compares his results with a set of experimental results obtained for a rail of a finite length, without reference to the existing analytic solutions and without confirming the accuracy of his solutions.

The accurate calculation of all the real and complex branches is necessary for a proper study of wave propagation in a rod of arbitrary cross-section. According to Saint Venant's Principle, in a waveguide of finite length, the influence of evanescent waves is increasingly noticeable for shorter lengths, or near the loads or ends. In an infinite waveguide, evanescent waves are important in the vicinity of loads. Guided by our general research interest in development of a NDE technique based on guided wave propagation in a finite beam, in this paper we develop techniques, and corresponding FEM code, to calculate the imaginary and complex, as well as the real branches of an arbitrary elastic waveguide. We first proceed to derive the theoretical background for method used here and in [6]. In Section 2, we assume the complex solution for displacement field, invoke the appropriate form of Hamilton's principle, and discretize the equations using the finite element method. Then we apply our numerical technique to a circular rod in order to test it by comparison with solutions to the analytic equations of Pochhammer-Chree. The dispersion curves obtained numerically are presented in Section 3, along with a study of the convergence of the numerical solutions to the exact values. Section 4 contains the final remarks and conclusions. The derivations of Pochhammer-Chree equations and the finite element formulation are left for the Appendices.

2. PROBLEM FORMULATION

We consider an infinite free beam of isotropic elastic material and constant cross-section, extending along z -axis while in reference state (Fig. 1), with a traction-free lateral surface. At any point along an unforced span of the beam, the vibration at a frequency ω is governed by a 3-D wave equation and results with a *complex displacement field* that can be written, without the loss of generality, as a discrete superposition of waves in the following form [1-6]:

$$\begin{aligned}
 \mathbf{u}(x, y, z, t) &= u(x, y) \mathbf{e}^{i\omega t - ikz} \\
 \mathbf{v}(x, y, z, t) &= v(x, y) \mathbf{e}^{i\omega t - ikz} \\
 \mathbf{w}(x, y, z, t) &= w(x, y) \mathbf{i} \mathbf{e}^{i\omega t - ikz},
 \end{aligned} \tag{2.1}$$

where k is the wave number and $u(x, y)$, $v(x, y)$ and $w(x, y)$ are real displacement amplitudes of the elastic waves traveling in positive z -direction with a phase velocity equal to ω/k . The phase shift of $\pi/2$ between transverse displacement fields and the longitudinal displacement field, introduced by the factor of i in the definition of w , is arbitrary, but chosen for later convenience since it ultimately leads to real coefficients in the governing equation.

For the circular rod, there exist closed form analytic frequency equations known as Pochhammer-Chree equations, relating k and ω . In order to consider linear vibrations of a beam with arbitrary cross-section, we must resort to one of the approximate methods. Hamilton's Principle naturally comes to mind on two counts. First, it states the conditions for the admissible displacement field (in dynamic equilibrium) that must be met only in the average sense, thereby allowing the use of an approximating displacement field that is defined in piece-wise fashion, with finite number of degrees of freedom (d.o.f.). For the case of continuous displacement field, the necessary and sufficient conditions on all the admissible configurations require [7] that the time integral of the *Lagrangian* – a functional that implicitly contains the wave equation that describes the problem – is stationary for the actual locus of configurations during the interval $[t_1, t_2]$:

$$\delta \int_{t_1}^{t_2} L dt = 0 \tag{2.2}$$

Secondly, we can benefit from the existence of eigenvalue bounding theorems and corresponding monotonic convergence of the approximate methods that build upon this principle.

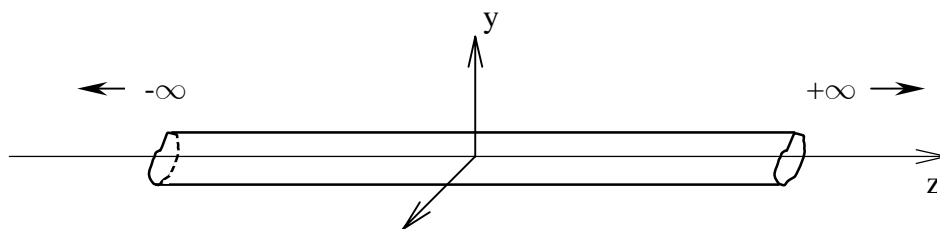


Figure 1. Infinite waveguide

However, since the functional of interest, as a form of energy, must be real, we cannot apply the Hamilton's Principle as defined in conventional elastodynamics, because our admissible displacement field (2.1) is complex. We can still locate the stationary points of the time integral of the contributions of all the admissible configurations to the Lagrangian, as long as the sum of those contributions yields a real Lagrangian. In the following chapter, we define the *Lagrangian* and formulate *Hamilton's Principle for complex fields*.

2.1. Hamilton's Principle for complex fields

Here we temporarily adopt the index notation such that u_q represent u , v and w components of some admissible displacement field, and x_q represent the Cartesian coordinates x , y and z . In general, the Lagrangian is equal to an integral over the volume of the difference between the kinetic energy of the system and total potential energy (sum of strain energy and potential energy of the forces), which for this problem amounts to:

$$L = \iiint_V \left(\frac{1}{2} \rho \dot{u}_q \dot{u}_q - \frac{1}{2} (\lambda \epsilon_{rr} \epsilon_{pp} + 2\mu \epsilon_{qp} \epsilon_{qp}) \right) dV \quad (2.3)$$

where the dot denotes first derivative w.r.t. time and λ and μ are Lamé constants (functions of Young's modulus E and Poisson's ratio ν). Upon substituting the strain tensor for small deformations, $\epsilon_{qp} = (\mathbf{u}_{q,p} + \mathbf{u}_{p,q})/2$, where $\mathbf{u}_{q,p} = \partial \mathbf{u}_q / \partial x_p$, the functional can be fully expressed in terms of only the displacements and their first temporal and spatial derivatives.

For a Lagrangian of the above form, being a quadratic functional of *real displacement fields*,

$$L = L(\dot{u}_q \dot{u}_q, u_{q,p} u_{r,s}), \quad (2.4)$$

we may generalize to the case of *complex displacement fields* by replacing all quadratic terms in (2.4) with the product of displacements (or derivatives of displacements) and appropriate complex conjugates, i.e.,

$$L = L(\dot{u}_q \dot{u}_q^*, u_{q,p} u_{r,s}^*), \quad (2.5)$$

where the star denotes a complex conjugate. Each product loses the imaginary unit and the entire functional can be rewritten as the sum of conventional Lagrangians of the real and the imaginary part of the displacement field, i.e.,

$$L = L(\text{Re}(\mathbf{u}_p)) + L(\text{Im}(\mathbf{u}_p)). \quad (2.6)$$

It is safe then to apply the Hamilton's Principle:

$$\delta \int_{t_1}^{t_2} L dt = 0, \quad (2.7)$$

which then gives 2 solutions for each stationary point – one for $\text{Re}(\mathbf{u}_p)$ and one for $\text{Im}(\mathbf{u}_p)$. After substituting the complex displacement field, Eqns. (2.1), the complex exponentials with t - and z -dependence cancel out, and we arrive at the *weak statement* of the problem:

$$\delta \iint_{\Omega} \frac{1}{2} (\kappa_2(x, y) k^2 + \kappa_1(x, y) k + \kappa_0(x, y) - \mathfrak{M}(x, y) \omega^2) d\Omega = 0 \quad (2.8)$$

where

$$\kappa_2(x, y) = \frac{E}{2(1+\nu)} (u^2 + v^2) + \frac{(1-\nu)E}{(1+\nu)(1-2\nu)} w^2 \quad (2.9)$$

$$\kappa_1(x, y) = \frac{2\nu E}{(1+\nu)(1-2\nu)} w \left(\frac{\partial u}{\partial x} + \frac{\partial v}{\partial y} \right) - \frac{E}{1+\nu} \left(\frac{\partial w}{\partial y} \nu + \frac{\partial w}{\partial x} u \right) \quad (2.10)$$

$$\begin{aligned} \kappa_0(x, y) = & \frac{E}{(1+\nu)(1-2\nu)} \left(\left(\frac{\partial u}{\partial x} \right)^2 + \left(\frac{\partial v}{\partial y} \right)^2 - \nu \left(\frac{\partial u}{\partial x} - \frac{\partial v}{\partial y} \right)^2 \right) + \\ & + \frac{E}{2(1+\nu)} \left(\left(\frac{\partial w}{\partial x} \right)^2 + \left(\frac{\partial w}{\partial y} \right)^2 + \left(\frac{\partial u}{\partial y} - \frac{\partial v}{\partial x} \right)^2 \right) \end{aligned} \quad (2.11)$$

correspond to the parts of total potential energy, while

$$\mathfrak{M}(x, y) = \rho (u^2 + v^2 + w^2) \quad (2.12)$$

corresponds to the kinetic energy of the body, noting again that u , v and w are the factors appearing in (2.1) and depend solely on x and y . Due to the waveguide's translational invariance in both time and z , the deformation of the entire waveguide is sufficiently described by the 3-D deformation of the cross-section, for each ω and k .

In order to introduce the *discrete displacement field* in the following chapter, we first set

$$\alpha = \frac{E}{(1+\nu)(1-2\nu)} \quad \text{and} \quad \beta = \frac{E}{2(1+\nu)}, \quad (2.13)$$

and then rewrite Eqn. (2.8) in matrix form:

$$\begin{aligned} \delta \iint_{\Omega} \frac{1}{2} \left(\{u\}^T [\kappa_2] \{u\} k^2 + (\partial \{u\})^T [\kappa_1] \{u\} k + (\partial \{u\})^T [\kappa_0] \partial \{u\} - \right. \\ \left. - \{u\}^T [\mathfrak{M}] \{u\} \omega^2 \right) d\Omega = 0 \end{aligned} \quad (2.14)$$

where

$$[\kappa_2] = \begin{bmatrix} \beta & 0 & 0 \\ 0 & \beta & 0 \\ 0 & 0 & (1-\nu) \alpha \end{bmatrix}, \quad (2.15)$$

$$[\kappa_1] = \begin{bmatrix} 0 & 0 & 2\nu\alpha \\ 0 & 0 & 0 \\ 0 & 0 & 0 \\ 0 & 0 & 2\nu\alpha \\ -2\beta & 0 & 0 \\ 0 & -2\beta & 0 \end{bmatrix}, \quad (2.16)$$

$$[\kappa_0] = \begin{bmatrix} (1-\nu)\alpha & 0 & 0 & \nu\alpha & 0 & 0 \\ 0 & \beta & \beta & 0 & 0 & 0 \\ 0 & \beta & \beta & 0 & 0 & 0 \\ \nu\alpha & 0 & 0 & (1-\nu)\alpha & 0 & 0 \\ 0 & 0 & 0 & 0 & \beta & 0 \\ 0 & 0 & 0 & 0 & 0 & \beta \end{bmatrix}, \quad (2.17)$$

$$[\mathfrak{M}] = \begin{bmatrix} \rho & 0 & 0 \\ 0 & \rho & 0 \\ 0 & 0 & \rho \end{bmatrix}. \quad (2.18)$$

Vector $\{u\}$ represents the displacement vector of a point on the cross-section, with components u , v and w and $\partial\{u\}$ is a six-component column vector, composed of the x- and y-derivatives of $\{u\}$.

2.2. FE Formulation

We replace the continuous cross-section with a mesh of 3-noded triangles, and replace the set of admissible continuous displacement fields $\{u(x, y)\}$ for each element, with the approximate field $\{\tilde{u}^e(\xi, \eta)\} = [N(\xi, \eta)]\{d^e\}$. The three degrees of freedom (nodal displacements) per each node are contained in $\{d^e\}$ and the shape functions for that element are contained in matrix $[N(\xi, \eta)]$, which is of order 3×9 . These linear, constant-strain elements satisfy the continuity requirement C^0 imposed by the highest-order derivative in the functional (2.5). Their shape functions interpolate the displacement field values linearly between the nodes, resulting in continuity of displacement field between the elements, and discontinuity of its derivatives of order 1 and higher. Furthermore, we use the same shape functions for interpolation of both the nodal coordinates and the nodal displacements (*isoparametric elements*) [9]. With the details of the derivations left in Appendix A.1, the finite element formulation of our problem becomes:

$$([\mathbf{K}_2] k^2 + [\mathbf{K}_1] k + [\mathbf{K}_0] - [\mathbf{M}] \omega^2)\{d\} = \{0\}, \quad (2.19)$$

where $\{d\}$ is the global displacement vector containing all degrees of freedom (d.o.f.), and $[K_2]$, $[K_1]^*$, $[K_0]$ and $[M]$ are global matrices assembled from the element matrices $[\kappa_2]$, $[\kappa_1]$, $[\kappa_0]$ and $[\mathfrak{M}]$ integrated over corresponding element area using 3-point Gauss quadrature. They are all real and symmetric and of order N , equal to the total number of d.o.f. used in approximation, i.e., three times the number of nodes.

The objective is to find the wave numbers k that satisfy the Eqn. (2.19). Simple examination of this equation reveals that, since the expression in parentheses is quadratic in k and the matrices are of order N , the vanishing determinant gives a polynomial of order $2N$. Therefore, there should be $2N$ solutions for k , and they are generally distinct (providing there is no degeneracy) and complex. The solutions should also come in pairs of complex conjugates[†]. Furthermore, if some k is a solution, then $-k$ should also be a solution[‡] due to the parity symmetry in z .

That the wavenumbers k and, correspondingly, the vectors $\{d\}$ should be complex in general, may appear to be inconsistent with the assumption used in derivation of Eqn. (2.19). That there is no inconsistency and that the complex solutions of (2.19) are meaningful, may be established using concepts of analytic continuation.

For $k=0$, Eqn. (2.19) reduces to a generalized eigenvalue problem (EVP) with real, symmetric, positive-definite matrices:

$$([K_0] - [M] \omega^2) \{d\} = \{0\}. \quad (2.20)$$

The eigenvalues $\pm \omega_{c.o.}$ are real and are known in elastodynamics as cutoffs – the frequencies at which some of the evanescent waves (imaginary branches) become propagative (real branches) and all the points of the waveguide vibrate in phase. Much is known about the convergence of solutions of generalized EVPs. Most notably, the Eigenvalue Separation Theorem [8] claims that, for the complete approximation space, the eigenvalues of the $N+1$ d.o.f. model bracket the eigenvalues of the N d.o.f. model and, therefore, as N increases, the approximate eigenvalues approach the actual eigenvalues asymptotically and from above (since the actual eigenvalues are lower bounds for approximate ones). However, there is no similar postulation for the evanescent waves, which appear together with propagating waves in the case of our full-fledged problem, $k \neq 0$ in Eqn.(2.19). In order to benefit somewhat from the abovementioned theorem, we proceed by drawing a parallel between our problem and the generalized EVP.

In a manner that bears similarity to the state space reformulation of dynamics, we rewrite the Eqn. (2.19) in the form of a generalized EVP. We introduce a new vector:

$$\{\psi\} = k \{d\} \quad (2.21)$$

* actually, the symmetric part of $[K_1]$ (see Appendix A.1)

† The complex roots of any polynomial with real coefficients always come in pairs of complex conjugates.

‡ The waves going to the left are the same as the waves going to the right, so the solution pair $(-k; u, v, -w)$ gives the mirror image of the wave represented by the solution pair $(k; u, v, w)$.

and multiply it with the matrix $[K_2]$, chosen for later convenience:

$$[K_2]\{\psi\} = k[K_2]\{d\}. \quad (2.22)$$

Since $[K_2]$ is non-singular, the above multiplication incurs no loss of information. Combining Eqns. (2.19) and (2.22) we obtain:

$$\begin{bmatrix} [K_2] & [0] \\ [0] & \omega^2[M] - [K_0] \end{bmatrix} \begin{Bmatrix} k\{d\} \\ \{d\} \end{Bmatrix} = k \begin{bmatrix} [0] & [K_2] \\ [K_2] & [K_1] \end{bmatrix} \begin{Bmatrix} k\{d\} \\ \{d\} \end{Bmatrix}. \quad (2.23)$$

Both $2N \times 2N$ matrices are real and symmetric (symmetry of the matrix on the right hand side ensured by the choice of $[K_2]$ in (2.22)), although not positive-definite. Just like our original problem, this equation has $2N$ distinct, generally complex solutions.

2.3. FE Mesh

We use TRIANGLE**, a 2-D Quality Mesh Generator and Delaunay Triangulator to create a mesh of 3-noded triangles with specified maximum area and no angles smaller than 33.8° . Even though in this paper we present a method for treating waveguides of arbitrary cross-section, we choose the circular cross-section for the purpose of comparison with the Pochhammer-Chree analytic solutions outlined in Appendix A.2.

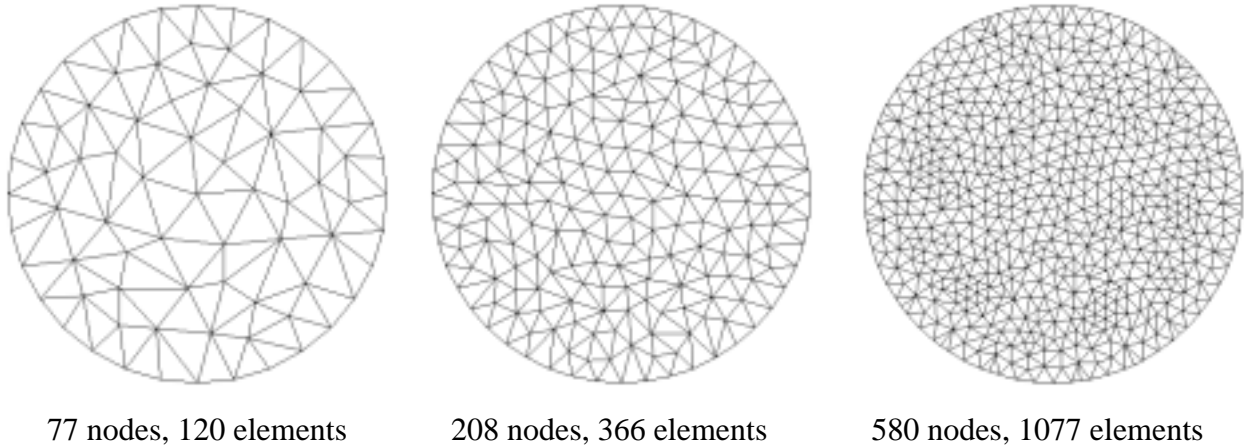


Figure 2. Representative FE meshes

TRIANGLE does not ensure symmetry and uniformity of the mesh it generates, and we used that here as a convenient check for accuracy. The symmetry of the circular rod assures that, except

** Copyright 1996 Jonathan Richard Shewchuk, SCS, Carnegie Mellon University

for the axi-symmetric waves, the modes must have two-fold degeneracy, related to sines and cosines, equivalent to clock-wise and counter clock-wise going waves and, therefore, solutions for k must occur in identical pairs. Since our meshes are not symmetric, normally identical k values should be slightly different, so their closeness demonstrates the level of accuracy.

Table 1. Mesh characteristics

No.	# of nodes	# of elements	$A_{\text{elt. max}}$ [% A_{total}]	h [cm]
1	77	120	1.41	0.2619
2	123	204	0.85	0.1905
3	208	366	0.42	0.1468
4	308	558	0.28	0.1269
5	580	1077	0.14	0.0793

Along with meshes in Fig. 2, we also used 2 intermediate meshes: one with 123 nodes and 204 elements, and the other with 308 nodes and 558 elements (Table 1), all characterized by maximum element area $A_{\text{elt. max}}$ and characteristic element length h . We refined the mesh by both decreasing $A_{\text{elt. max}}$ and increasing the number of nodes. In addition to that, we used several very coarse meshes for initial qualitative study of root degeneracy. The radius of the circle is $a = 1.5$ cm and all the lengths are in cm.

3. DISPERSION CURVES

In order to obtain more general feel for the quality of our numerical results, we use the same dimensionless variables and constants as introduced in development of the Pochhammer-Chree equations (Appendix 2). Additionally, we choose dimensionless Young's modulus $E=1$ and dimensionless density $\rho=1$, so that the bar speed is $c_b = \sqrt{E/\rho} = 1$. The Poisson's ratio is $\nu = 0.3$.

In our Fortran computer code we search for dimensionless wavenumber \bar{k} given the dimensionless frequency $\Omega = \omega a / c_2$, in densely spaced steps of $\Delta\Omega = 0.02$. The procedure may be contrasted with a method that chooses \bar{k} , and solves a more standard EVP for Ω . Our choice of method is informed by perspective based on anticipated experiments, in which frequencies are specified by the loading, and the responses (i.e., \bar{k} 's) are measured. Furthermore, the expected sparseness of imaginary \bar{k} values associated with moderate Ω 's, and the inability to guess complex \bar{k} 's associated with real Ω 's, renders the latter approach unworkable. We used that procedure to calculate the branches (solve Eqn. (2.23)), using a NAG Fortran library routine that computes all the eigenvalues of the generalized EVP of the form $\mathbf{Ax} = \lambda\mathbf{Bx}$, where \mathbf{A} and \mathbf{B} are real, square, but not necessarily positive-definite matrices. For the problem of calculating the cutoffs, we used similar but more specialized routine that computes all the eigenvalues of a real symmetric-definite generalized EVP.

The wavenumbers obtained in our code come, as expected, mostly in doubles, except for a few singles. The purely real and purely imaginary solutions also come in pairs of opposite signs, and the fully complex ones come in quads of complex conjugates.

The resulting dispersion curves are shown in Fig. 3. We chose to present the results for the coarsest mesh because the two-fold degeneracy of all but axi-symmetric waves is the most obvious in that case. The branches that would be coinciding if the mesh were symmetric, are apart here – more so for higher order branches, which is clear in the example of, say, imaginary branches B_1 and B_2 . For finer meshes the difference between two branches in a pair is diminishing and cannot be discerned on the graph of the same bounds as the one in Fig. 3. On the other hand, further coarsening of the mesh has proven to result with many or even most of the branches missing, especially higher ones that are in the densely weaved regions – we will come back to that issue in our study of convergence in the next sub-section.

We calculated all the cutoffs and branches up to $\Omega = 6.419$ (4th flexural cutoff) and compared them with the Pochhammer-Chree solutions for $n = 0 \div 5$. The absolute error of our solution, for the chosen meshes, is less than 2 % for any point in the region presented in Fig.3 and the exact curves fall on top of our approximate ones. We refrained from plotting them together for the sake of clarity.

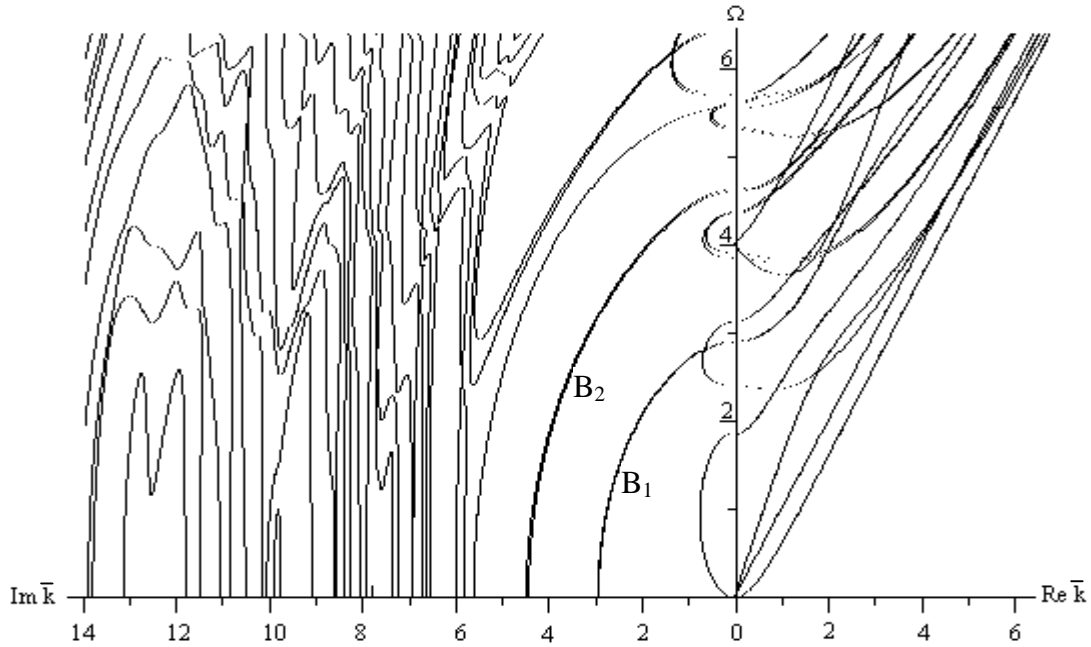


Figure 3. Dispersion curves for the coarsest mesh – real and imaginary branches

There are 3 propagating modes below the first cutoff – longitudinal, torsional and 2 degenerate flexural modes that are located in the $\text{Re } \bar{k} - \Omega$ quadrant, Fig.3. The remaining solutions are pure imaginary or complex. We plotted only imaginary and real branches. It is possible to

include the complex branches in a 3-D plot with axes $\text{Re}\bar{k}$, $\text{Im}\bar{k}$ and Ω , but the extreme intricacy of the detail of such a plot is beyond the scope of this paper. In a simple examination of the complex solution data, we located the exact longitudinal and flexural modes corresponding to the lowest complex modes obtained by the code and we found them in good agreement (quantitative assessment is given in the following sub-section).

3.1. Accuracy and convergence

Since the 3-noded triangles used in this study have 1st order polynomial interpolation functions, the appropriate mesh fineness parameter is $1/h$, where h is a characteristic length of the worst element (the element with the greatest surface area and/or sharpest angle). One can argue that the truly critical parameter involves the resolution across the cross-section, so the representative mesh parameters are $\frac{1}{\alpha/h}$ and $\frac{1}{\beta/h}$, where α and β are transverse wavenumbers from (A.2.6).

However, the transverse wavenumbers can be 0 for some combinations of k and ω , so for general purpose it is convenient to leave them out. We choose to evaluate the convergence of our solutions by noting the dependence of the absolute error of the frequency (for cutoffs) and wavenumbers (for branches) on $\frac{1}{h}$, both in terms of natural logarithm. In a plot of $\ln |\Omega - \Omega_{\text{exact}}|$

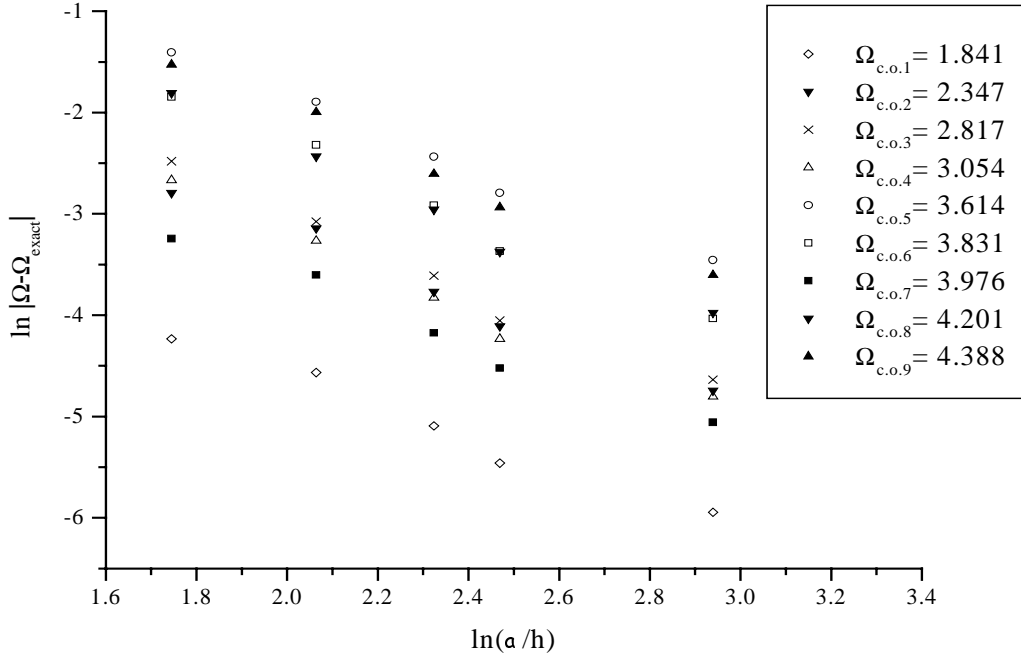


Figure 4. Numerical convergence of the first 9 cutoffs

versus $\ln\left(\frac{1}{h}\right)$, the rate of convergence of cutoffs is equal to the slope of the convergence curve s , and it represents the rate at which the accuracy of the solution increases with the mesh refinement:

$$|\Omega - \Omega_{\text{exact}}| \sim \left(\frac{1}{h}\right)^s \quad \text{and, similarly} \quad |\bar{k} - \bar{k}_{\text{exact}}| \sim \left(\frac{1}{h}\right)^s. \quad (3.1)$$

Furthermore, the vertical position of the convergence curve is the measure of accuracy of that particular solution.

We checked the convergence of cutoffs for first 9 cutoffs obtained by the code (Fig. 4). All the cutoffs are converging to the exact value with similar rate ($s = (-1.5) \div (-1.7)$). However, there is no apparent ordering of levels of accuracy according to the cutoff order. Furthermore, no ordering exists even within the families of branches with the same azimuthal order – it appears that, only for some n -families, the accuracy is lower for the higher branches as might be suggested by the intuition.

In order to present the convergence of the branches in this paper, we chose to consider the lower real, imaginary and complex solutions for a single frequency, $\Omega = 1.0$.

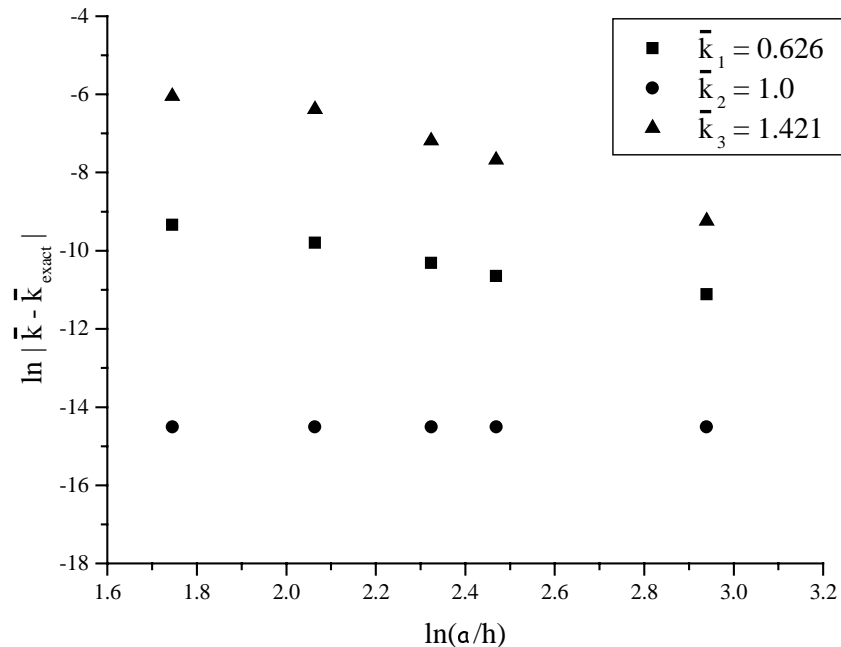


Figure 5. Numerical convergence of the selected real branches

The convergence of solutions for real branches is studied only in the case of three branches that exist below the first cutoff – longitudinal, torsional and flexural modes (Fig. 5). The torsional mode (the lowest data set) is almost exact, with practically 0 convergence rate, since it does not improve with mesh refinement. The longitudinal mode (middle data set) is more accurate but it is converging more slowly than the flexural mode (upper data set) with $s = -1.5$, as opposed to $s = -2.7$ for the flexural.

From the solutions for purely imaginary branches, we choose one high value for the purpose of demonstrating the effect of higher orders on the accuracy of the solution. One can notice (Fig.6) that a value for the coarsest mesh is missing for the highest mode – we were not able to determine what solution from our code corresponds to this Pochhammer-Cree solution. Note that the analytic branches are grouped according to the azimuthal order n , while our code sorts the solutions in the ascending order of absolute value (case of purely real or imaginary solutions)

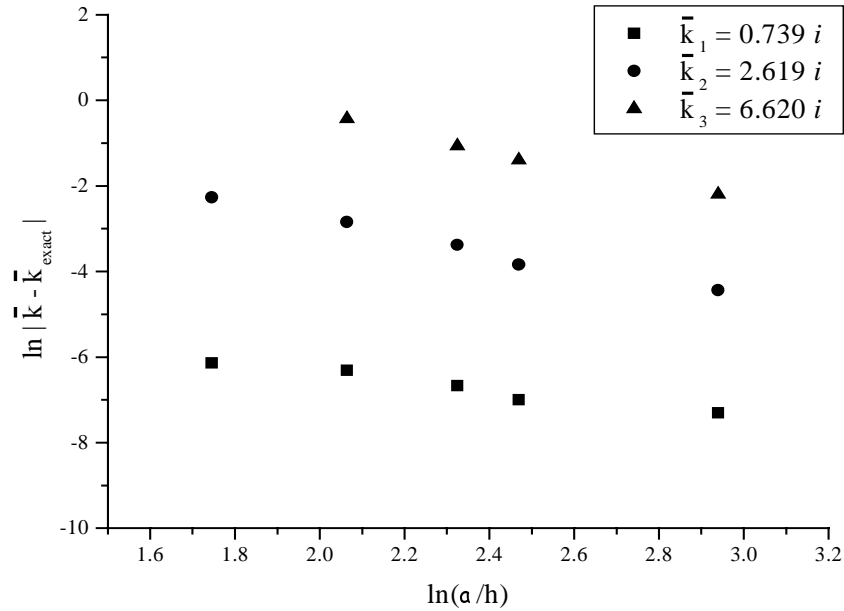


Figure 6. Numerical convergence of the selected imaginary branches

or modulus (in case of complex solutions). There is no consistent method of correlating the points on the numerically and analytically obtained branches, and for very coarse meshes and higher order branches, it becomes increasingly difficult to recognize the corresponding roots. Aside from that, these 3 branches certainly prove that the accuracy decreases for higher order branches, but nothing general can be inferred from that. The rate of convergence of the selected imaginary branches is $s = (-1.1) \div (-1.9)$.

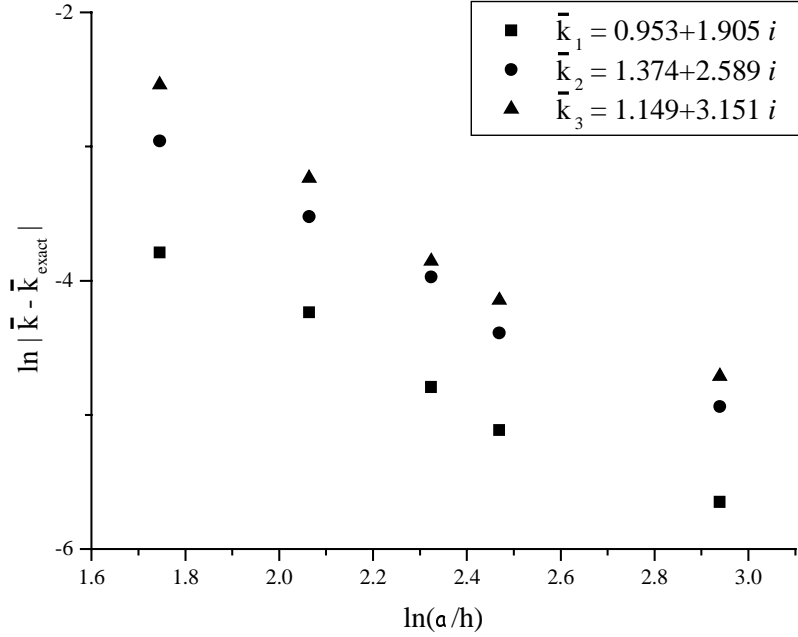


Figure 7. Numerical convergence of the selected complex branches

In order to easily locate the complex branches, we used our code's lowest three solutions as starting guesses for the Newton-Raphson method of root searching of the Pochhammer-Chree equations, trying different values of azimuthal order n . The method located the corresponding Pochhammer-Chree solutions for $n = 2, 0$ and 3 respectively (Fig.7). The accuracy of those solutions is good, but somewhat lower than for real and purely imaginary branches. The convergence rate is $s = (-1.6) \div (-1.8)$, somewhat faster for flexural than for longitudinal mode.

Finally, we revisit the question of the mesh coarseness and the limitations it poses in the sense of accuracy of solutions. FEM solution is inaccurate when the wavelength of the propagating waves becomes comparable to mesh size. The rough criterion of accuracy w.r.t. mesh coarseness can be formulated as:

$$\frac{\omega}{c_2} \ll \frac{1}{h} \quad (3.2)$$

and in terms of dimensionless variables, it becomes:

$$\Omega \frac{a}{h} \ll 1. \quad (3.3)$$

This criterion gives the idea of how many branches intersected by the chosen Ω give meaningful results for the chosen mesh. Therefore, the higher we go in frequency, the finer mesh we will need in order to get acceptable accuracy.

4. CLOSURE

We have developed a code for the calculation of wave propagation in an elastic waveguide of arbitrary cross-section. It is capable of accurately determining the real, imaginary and complex branches at moderate values of dimensionless frequency and wavenumber, as demonstrated by comparison with known solutions in the circular waveguide. More detailed comparison of analytical and our numerical results for complex branches are needed for further understanding of the behavior of complex branches – do they connect minima and maxima of all the branches or only of longitudinal ones (as shown by Onoe *et al.*). Does this distribution of solutions into few real, many imaginary and vast number of complex branches, appear in the arbitrary cross-sections and for different values of Poisson's ratio, or some types of branches cease to exist?

We anticipate applications of this method to waveguides with various common cross-sections, such as railroad rails and rectangular waveguides, in particular to the non-destructive assessment of contained stress and anisotropy in rail.

ACKNOWLEDGEMENTS

This work was supported by the Association of American Railroads Technical Scanning Committee, and by the National Computational Science Alliance which provided resources on its Silicon Graphics Origin2000.

APPENDICES

A.1. Derivation of FE formulation

First we introduce isoparametric mapping for 3-noded triangle – the same shape functions both for coordinates and the displacements [9]:

$$\begin{aligned}x(\xi, \eta) &= \sum_{i=1}^3 x_i N_i(\xi, \eta) \\y(\xi, \eta) &= \sum_{i=1}^3 y_i N_i(\xi, \eta),\end{aligned}\tag{A.1.1}$$

where x_i and y_i are the nodal coordinates of the element. The above expressions specify x and y coordinates of any point in the triangle in terms of the parameters ξ and η , such that $0 \leq \eta \leq 1$ and $0 \leq \xi \leq 1 - \eta$. Similarly, the displacements at any point (ξ, η) are:

$$\begin{aligned}u(\xi, \eta) &= \sum_{i=1}^3 u_i N_i(\xi, \eta) \\v(\xi, \eta) &= \sum_{i=1}^3 v_i N_i(\xi, \eta) \\w(\xi, \eta) &= \sum_{i=1}^3 w_i N_i(\xi, \eta),\end{aligned}\tag{A.1.2}$$

where u_i , v_i and w_i are the nodal displacements. The shape functions are:

$$\begin{aligned}N_1 &= 1 - \xi - \eta \\N_2 &= \xi \\N_3 &= \eta.\end{aligned}\tag{A.1.3}$$

Then the approximate displacement field within the element is:

$$\{\tilde{u}^e(\xi, \eta)\} = [N(\xi, \eta)]\{d^e\},\tag{A.1.4}$$

where

$$\{d^e\} = \{u_1 \ v_1 \ w_1 \ u_2 \ v_2 \ w_2 \ u_3 \ v_3 \ w_3\}^T,\tag{A.1.5}$$

$$[N(\xi, \eta)] = \begin{bmatrix} N_1 & 0 & 0 & N_2 & 0 & 0 & N_3 & 0 & 0 \\ 0 & N_1 & 0 & 0 & N_2 & 0 & 0 & N_3 & 0 \\ 0 & 0 & N_1 & 0 & 0 & N_2 & 0 & 0 & N_3 \end{bmatrix}. \quad (\text{A.1.6})$$

In addition to that, the displacement gradients are approximated with:

$$\partial\{\tilde{u}^e\} = [D]\{\tilde{u}^e\} = [D][N]\{d\}, \quad (\text{A.1.7})$$

where $[D]$ is merely the operator matrix:

$$[D] = \begin{bmatrix} \partial/\partial x & 0 & 0 \\ \partial/\partial y & 0 & 0 \\ 0 & \partial/\partial x & 0 \\ 0 & \partial/\partial y & 0 \\ 0 & 0 & \partial/\partial x \\ 0 & 0 & \partial/\partial y \end{bmatrix}. \quad (\text{A.1.8})$$

It operates on $[N]$, resulting in:

$$[B] = [D][N] = \begin{bmatrix} [J]^{-1} \\ [J]^{-1} \\ [J]^{-1} \end{bmatrix} \begin{bmatrix} N_{1,\xi} & 0 & 0 & N_{2,\xi} & 0 & 0 & N_{3,\xi} & 0 & 0 \\ N_{1,\eta} & 0 & 0 & N_{2,\eta} & 0 & 0 & N_{3,\eta} & 0 & 0 \\ 0 & N_{1,\xi} & 0 & 0 & N_{2,\xi} & 0 & 0 & N_{3,\xi} & 0 \\ 0 & N_{1,\eta} & 0 & 0 & N_{2,\eta} & 0 & 0 & N_{3,\eta} & 0 \\ 0 & 0 & N_{1,\xi} & 0 & 0 & N_{2,\xi} & 0 & 0 & N_{3,\xi} \\ 0 & 0 & N_{1,\eta} & 0 & 0 & N_{2,\eta} & 0 & 0 & N_{3,\eta} \end{bmatrix}, \quad (\text{A.1.9})$$

where $[J]^{-1}$ is the inverse of the Jacobian:

$$[J] = \begin{bmatrix} \frac{\partial x}{\partial \xi} & \frac{\partial y}{\partial \xi} \\ \frac{\partial x}{\partial \eta} & \frac{\partial y}{\partial \eta} \end{bmatrix}. \quad (\text{A.1.10})$$

Noting that $d\Omega^e = dx dy = \det[J] d\xi d\eta$, we finally arrive at the discretized form of the functional in Eqn. (2.14) for one element:

$$\Pi^e = \frac{1}{2} \{d^e\}^T \left[\int_0^1 \int_0^{1-\eta} \left(k^2 [N]^T [\kappa_2] [N] + k [B]^T [\kappa_1] [N] + [B]^T [\kappa_0] [B] - \omega^2 [N]^T [\mathfrak{M}] [N] \right) \det[J] d\xi d\eta \right] \{d^e\}. \quad (\text{A.1.11})$$

The integral in square brackets is a 9×9 *local matrix*, whose elements are placed in the *global matrix*, let us call it $[G]$, according to the corresponding d.o.f. numbers and we obtain the global functional, which is of the form:

$$\begin{aligned} \Pi^\Omega &= \frac{1}{2} \{d\}^T \left([K_2] k^2 + [K_1] k + [K_0] - [M] \omega^2 \right) \{d\} = \\ &= \frac{1}{2} \{d\}^T [G] \{d\} = \frac{1}{2} d_i G_{ij} d_j. \end{aligned} \quad (\text{A.1.12})$$

We note that all matrices that comprise $[G]$, *except* $[K_1] k$, are explicitly symmetric matrices. Now we look for the stationary points of this energy functional over the restricted space spanned by all the possible vectors $\{d\}$. At stationary points, the first derivative w.r.t. the displacement field must vanish,

$$\frac{\partial \Pi^\Omega}{\partial d_i} = \frac{\partial}{\partial d_i} \left(\frac{1}{2} d_i G_{ij} d_j \right) = \frac{1}{2} (G_{ij} + G_{ji}) d_j = 0, \quad (\text{A.1.13})$$

which gives:

$$\text{sym}[G] \{d\} = \left([K_2] k^2 + \text{sym}[K_1] k + [K_0] - [M] \omega^2 \right) \{d\} = \{0\}. \quad (\text{A.1.14})$$

Thus we arrive to Eqn. (2.19).

A.2. Analytic solution: Pochhammer-Chree equations

The displacement field associated with harmonic waves in a solid cylindrical rod infinite in z -direction and of radius a , formulated in terms of potential functions Φ and \mathbf{H} , can be written as [1- 5]:

$$\mathbf{u} = \nabla \Phi + \nabla \times \mathbf{H}, \quad (\text{A.2.1})$$

with $\mathbf{u} = (u_\theta, u_r, u_z)$, $\mathbf{H} = (H_\theta, H_r, H_z)$, and

$$\nabla \cdot \mathbf{H} = F(\mathbf{r}, t)^*. \quad (\text{A.2.2})$$

* Function $F(\mathbf{r}, t)$ is arbitrary, due to gauge invariance of the Helmholtz resolution (A.2.1).

The conditions of momentum balance and Hooke's law for isotropic material, require that potentials Φ and \mathbf{H} satisfy the scalar and vector wave equation respectively:

$$\nabla^2 \Phi = \frac{1}{c_1^2} \frac{\partial^2 \Phi}{\partial t^2} \quad \text{and} \quad \nabla^2 \mathbf{H} = \frac{1}{c_2^2} \frac{\partial^2 \mathbf{H}}{\partial t^2}. \quad (\text{A.2.3})$$

The longitudinal (dilatational) and shear (distortional) wave speeds are, respectively, $c_1 = \sqrt{(\lambda + 2\mu)/\rho}$ and $c_2 = \sqrt{\mu/\rho}$. Solutions are found by separation of variables into r -, θ - and z, t -dependence. For Φ and all 3 components of \mathbf{H} , the r -dependence contains Bessel functions of the 1st kind of order n and $n+1$, the θ -dependence is represented with $\sin(n\theta)$ and $\cos(n\theta)$, and the z, t -dependence is of the form $e^{i\omega t - ikz}$. By imposing traction-free boundary conditions, we obtain a system of 3 homogenous linear equations with 3 unknowns (the 4th unknown is set to 0 without loss of generality, due to the gauge invariance, see footnote below). In order to have a non-trivial solution the 3×3 determinant of coefficients has to vanish and, thus, we arrive at the transcendental equation that represents the *dispersion relation* for an infinite isotropic circular rod:

$$|a_{ij}| = 0, \quad (i, j = 1, 2, 3) \quad (\text{A.2.4})$$

where a_{ij} are the elements of a matrix of coefficients stemming from the boundary conditions. The coefficients depend, among other parameters, on the azimuthal order n . They are as follows [4,5]:

$$\begin{aligned} a_{11} &= \left\{ \frac{\lambda(\alpha^2 + \xi^2)(\alpha a)^2}{2\mu\alpha^2} + (\alpha a)^2 - n^2 \right\} J_n(\alpha a) + \alpha a J'_n(\alpha a) \\ a_{12} &= \left\{ n^2 - (\beta a)^2 \right\} J_n(\beta a) - \beta a J'_n(\beta a) \\ a_{13} &= 2n \left\{ \beta a J'_n(\beta a) - J_n(\beta a) \right\} \\ a_{21} &= n \left\{ \alpha a J'_n(\alpha a) - J_n(\alpha a) \right\} \\ a_{22} &= -n \left\{ \beta a J'_n(\beta a) - J_n(\beta a) \right\} \\ a_{23} &= - \left\{ 2n^2 - (\beta a)^2 \right\} J_n(\beta a) + 2\beta a J'_n(\beta a) \\ a_{31} &= -\alpha a J'_n(\alpha a) \\ a_{32} &= -\frac{\beta^2 - \xi^2}{2\xi^2} \beta a J'_n(\beta a) \\ a_{33} &= n J_n(\beta a), \end{aligned} \quad (\text{A.2.5})$$

where α and β are the ‘‘transverse’’ wavenumbers

$$\alpha^2 = \frac{\omega^2}{c_1^2} - k^2 \quad \text{and} \quad \beta^2 = \frac{\omega^2}{c_2^2} - k^2. \quad (\text{A.2.6})$$

For $n=0$, only a_{23} and its cofactor matrix remain non-zero, thus separating the torsional waves ($a_{23}|_{n=0} = 0$) and the longitudinal waves (determinant of the cofactor matrix vanishes). The resulting dispersion relation for torsional waves (only u_θ is non-zero) is:

$$(\beta a)^2 J_0(\beta a) = 2\beta a J_1'(\beta a) \quad (\text{A.2.7})$$

with solutions $\beta a = 0, 5.136, 8.417, 11.62, \dots$. Interestingly, the lowest mode of propagation of torsional waves ($\beta a = 0$) is the exceptional case where elasticity and strength of materials yield the same result, $\omega = c_2 k$.

The dispersion relation at $n=0$ for ‘‘longitudinal’’ waves (u_r and u_z are non-zero) is more complicated:

$$\bar{\alpha}(\bar{\beta}^2 + \bar{k}^2) J_1(\bar{\alpha}) J_1(\bar{\beta}) - (\bar{\beta}^2 - \bar{k}^2)^2 J_0(\bar{\alpha}) J_1(\bar{\beta}) - 4\bar{k}^2 \bar{\alpha} \bar{\beta} J_1(\bar{\alpha}) J_0(\bar{\beta}) = 0, \quad (\text{A.2.8})$$

with dimensionless wavenumber k and parameters α and β denoted with a bar:

$$\bar{\alpha} = \alpha a, \quad \bar{\beta} = \beta a \quad \text{and} \quad \bar{k} = k a. \quad (\text{A.2.9})$$

At $n \neq 0$ the determinant in (A.2.4) does not simplify and all the cases have a two-fold degeneracy represented by a rotation of the circular bar (sines and cosines in θ -dependence interchange), so the solutions come in pairs associated with $+n$ and $-n$ [§]. The lowest ‘‘flexural’’ modes (in the sense of strength of materials) are obtained for $n=1$. The resulting frequency equation is:

$$J_1(\bar{\alpha}) J_1^2(\bar{\beta}) (f_1 F_{\bar{\beta}}^2 + f_2 F_{\bar{\alpha}} F_{\bar{\beta}} + f_3 F_{\bar{\beta}} + f_4 F_{\bar{\alpha}} + f_5) = 0, \quad (\text{A.2.10})$$

where

$$F_x = x \frac{J_0(x)}{J_1(x)}, \quad (x = \bar{\alpha}, \bar{\beta}) \quad (\text{A.2.11})$$

are Onoe’s functions of the 1st kind of order 1 and

[§] That is not the case for $n=0$, where there is no θ -dependence in either Φ or components of \mathbf{H} . By substituting them in Eqns. (A.2.3), n^2 emerges and it always has two roots, $\pm n$, except for $n=0$.

$$\begin{aligned}
f_1 &= 2(\bar{\beta}^2 - k^2)^2 \\
f_2 &= 2\bar{\beta}^2(5k^2 + \bar{\beta}^2) \\
f_3 &= \bar{\beta}^6 - 10\bar{\beta}^4 - 2\bar{\beta}^4\bar{k}^2 + 2\bar{\beta}^2\bar{k}^2 + 2\bar{\beta}^2\bar{k}^4 - 4\bar{k}^4 \\
f_4 &= 2\bar{\beta}^2(2\bar{\beta}^2\bar{k}^2 - \bar{\beta}^2 - 9\bar{k}^2) \\
f_5 &= \bar{\beta}^2(-\bar{\beta}^4 + 8\bar{\beta}^2 - 2\bar{\beta}^2\bar{k}^2 + 8\bar{k}^2 - \bar{k}^4).
\end{aligned} \tag{A.2.12}$$

The literature has paid little attention to the $n>1$ case and its frequency equation remains the full-fledged Eqn. (A.2.4).

REFERENCES

- [1] J. Miklowitz, *Elastic Waves and Waveguides*
Series in Applied Mathematics and Mechanics, Vol. 22, North-Holland, 1978
- [2] Y. H. Pao, R.D. Mindlin, The Dispersion of Flexural Waves in an Elastic Circular Cylinder,
Part II, *Journal of Applied Mechanics*, Vol. 27, 1960
- [3] Y. H. Pao, The Dispersion of Flexural Waves in an Elastic Circular Cylinder, Part II
Journal of Applied Mechanics, Vol. 29, 1962
- [4] K. F. Graff, *Wave Motion in Elastic Solids*
Dover, 1991
- [5] T. R. Meeker, A. H. Meitzler, *Guided Wave Propagation in Elongated Cylinders and Plates*
Physical Acoustics, Vol. 1, Part A, Academic Press, 1964
- [6] L. Gavrić, Computation of Propagative Waves in Free Rail Using a Finite Element Technique
Journal of Sound and Vibration, Vol.185(3), 1995
- [7] C. L. Dym, I. H. Shames, *Solid Mechanics: A Variational Approach*
Advanced Engineering Series, McGraw-Hill, 1973
- [8] L. Meirovitch, *Fundamentals of Vibrations*
McGraw-Hill, 2001
- [9] R.D. Cook, D.S. Malkus, M.E. Plesha, *Concepts and Applications of Finite Element Analysis*
3rd Edition, John Wiley & Sons, 1989.